Volume 14
Number 20
31 March 2026
Pages 11799–12462

Journal of Materials Chemistry A

Materials for energy and sustainability

rsc.li/materials-a

ISSN 2050-7488

ROYAL SOCIETY OF **CHEMISTRY**

PAPER

Ayse Turak *et al.*

Sparse Au nanoparticle arrays modulate Zn nucleation pathways and ion transport: a mechanistic approach to dendrite-free aqueous battery cycling

Journal of
Materials Chemistry A

ROYAL SOCIETY
OF CHEMISTRY

PAPER

View Article Online
View Journal | View Issue

Check for updates

Cite this: *J. Mater. Chem. A*, 2026, **14**, 11975

Sparse Au nanoparticle arrays modulate Zn nucleation pathways and ion transport: a mechanistic approach to dendrite-free aqueous battery cycling

Seungil Lee,[a] Pedro Oliveira,[b] Mehdi Shamekhi,[a]
Raaja Rajeshwari Manickam,[a] Woo Young Kim,[c] Jong Hyun Lim[d] and Ayse Turak *[ab]

Received 5th October 2025
Accepted 6th January 2026

DOI: 10.1039/d5ta08137h

rsc.li/materials-a

Zinc-based rechargeable batteries are a promising low-cost alternative for grid-scale energy storage, but their lifetimes are limited by dendritic growth and side reactions at the metal anode. Here, we demonstrate a simple solution-based strategy to stabilize Zn anodes using a periodically sparse array of gold nanoparticles (Au NPs) deposited by reverse micelle templating. Unlike dense coatings or randomly aggregated particles, isolated Au NPs act as uniformly distributed nucleation sites that homogenize local charge fields, enhance ion transport, and suppress dendrite formation while preserving the active Zn surface. The process, achieved by gold-halide-loaded block copolymer micelles followed by plasma etching, provides precise nanoparticle size control and reproducible submonolayer coverage. Electrochemical testing shows reduced nucleation barriers, improved charge transfer kinetics, and markedly enhanced cycling stability, with symmetric cells exceeding 4000 hours of operation and delivering up to 50-fold lifetime improvements compared to bare Zn. Full-cell tests with V_2O_5 cathodes further confirm the improved efficiency and stability of Au NP-modified anodes. This work highlights nanoparticle decoration as a cost-effective and scalable interface engineering strategy for achieving long-life Zn batteries without compromising active surface area.

1 Introduction

Zinc-based energy storage technology has developed significant renewed attention due to its abundance, cost-effectiveness, low redox potential, stability and high specific volumetric capacity compared to other metal-based batteries.[1] Its potential applications span from portable electronics to electric vehicles and large-scale energy storage solutions. Specifically, zinc (Zn) ion batteries have emerged as potential sources for grid-scale stationary energy storage to cope with the demand for renewable energy plants that require suitable energy storage systems to produce electricity regardless of time and weather.[2]

However, challenges such as Zn dendrite growth, corrosion, and hydrogen evolution side reactions pose significant obstacles to their practical implementation by yielding low coulombic efficiency as well as low rechargeability.[3] The detrimental formation of dendrites during Zn plating can lead to protrusions that may puncture separators – causing short circuits – and detached protrusions can form "dead zinc" regions, reducing the amount of active material due to limited contact area and weak adhesion.[4,5]

To overcome these issues, incorporating artificial interphase protective layers seems the most promising strategy, by using electrolyte additives to form artificial layers within a few initial cycles or by direct deposition on the Zn foil.[6,7] A diverse range of interface layers have been developed using various materials, including inorganic metals and metal oxides such as Sn,[8] Ag,[9] $CaCO_3$,[10] and ZrO_2,[11] as well as polymers such as poly(2-vinylpyridine).[12] In particular, due to its high electrical conductivity and electrochemical stability, gold (Au) interlayers have been proposed as a highly stable interlayer material. Improved stability of Zn anodes with an Au protective layer deposited by magnetron sputtering was first reported by Cui *et al.*[13] and further investigated by Ren *et al.*[14] and Kim *et al.*[15] with great success in improving lifetimes and performance.

Such artificial interface films, focused on dense nanocoatings, serve either as physical barriers to prevent side reactions by blocking direct contact between Zn and the electrolyte or as regulators to enhance reaction kinetics, ensuring uniform ion distribution and electric fields, promoting uniform Zn deposition with high efficiency and stability.[6] However, during long-term operations, such protective layers are susceptible to significant volume fluctuations from continuous cycling, which may potentially result

---

[a] *Department of Physics, Centre for NanoScience Research (CeNSR), Concordia University, Montreal, Quebec, Canada. E-mail: ayse.turak@concordia.ca*
[b] *Department of Engineering Physics, McMaster University, Hamilton, Ontario, Canada*
[c] *A-PRO Materials Co., Ltd, Anyang, 14055, South Korea*
[d] *A-PRO Co., Ltd, Anyang, 14055, South Korea*

in cracks or layer detachment. Additionally, most interfacial layers are from several micrometers to hundreds of nanometers thick,[9,13,16,17] resulting in a large proportion of inactive materials and long migration distances for electrons and ions, thereby reducing specific capacity and increasing costs and interface resistance.[7,18]

In this study, we propose an alternative approach to interphase layers, by depositing a uniform sparse Au NP array to nanostructure the surface of Zn anodes using reverse micelle deposition (RMD). This facile, low-temperature, ambient solution-based process allows precise control over nanoparticle size and the formation of distinct 2D periodic patterns upon deposition, resulting in tunable surfaces.[19–23] We show that a structured, sparse nanoparticle array of periodically spaced Au NPs introduces distinct charge transport behaviors, improving electrode stability without the drawbacks of excessive surface coverage from thin Au films. The dispersion of isolated single Au NPs achieved through RMD prevents the aggregation of Au NPs from other synthesis methods that can create random sizes and distributions of unintentionally clumped Au particles, which would result in uneven charge distribution. As a result, uniformly dispersed zincophilic Au NPs are shown to act as distinct nucleation sites for Zn plating, preventing severe aggregation of Zn adatoms, supported by density functional theory (DFT) calculations. The sparse Au NP array differs fundamentally from both densely coated and unstructured nanoparticle surfaces, suppressing unwanted side reactions, while maintaining a large active Zn surface. The Au NP array distribution also homogenizes local electric fields on the surface and reduces energy barriers at the interface, creating an ion-pumping effect that promotes uniform ion transport along the surfaces. With those contributions, Zn electrodes modified with Au NPs demonstrate superior performance compared to those without Au NPs, showing higher stability than even the full coverage sputtered Au layers previously reported in the literature. Our proposed interlayer presents an alternative paradigm in interface engineering, where spatially controlled sparsity can be leveraged to enhance electrochemical stability and ion transport. Such an approach opens up new avenues for improving stability without sacrificing the active surface area for desirable reactions in battery technologies. While this study focuses on zinc electroplating during battery cycling, the underlying principles may extend to other fields.

2 Experimental details

2.1 Materials

Polystyrene-*b*-poly(2-vinyl pyridine) (PS(75 000)-*b*-P2VP(66 500)) was purchased from Polymer Source Ltd. Gold chloride hydrate ($HAuCl_4 \cdot 3H_2O$), *o*-xylene, and zinc sulfate heptahydrate ($ZnSO_4 \cdot 7H_2$) were purchased from Sigma-Aldrich and vanadium pentoxide (V_2O_5) slurry (80% of active material) coated stainless foil as a cathode was purchased from MSE supplies LLC. All materials were used as received without purification.

2.2 Preparation of the Au NP deposited Zn anode

A reverse micelle solution was prepared by dissolving the PS-*b*-P2VP diblock copolymer in *o*-xylene at a concentration of 3 mg ml^{-1}. After stirring for a minimum of 24 hours to form spherical reversed micelles, 0.5 M gold precursor solution composed of $HAuCl_4 \cdot 3H_2O$ dissolved in 2-propanol was sequentially added to the solution in specific loading ratios relative to the number of 2VP units. The stirring was continued for at least 48 hours at room temperature. The solution was then centrifuged and transferred to a clean vial to eliminate any precipitates. The Au-loaded reverse micelle solution was then deposited onto various substrates, including ⟨100⟩ Si wafers and zinc foil disks, with spin-coating at 2000 rpm. Subsequently, an O_2 plasma etching process was carried out under conditions of 950 mTorr and 29.6 W for 60 minutes to eliminate both the polymeric micelles and the residual solvents.

2.3 Characterization

The confirmation of nanoparticles and their size were analyzed using an atomic force microscope (AFM) (MultiMode 8-HR, Bruker, AFM) operating in scanasyst mode under ambient conditions, and the topography was analyzed using Gwydion software.[24] The morphology of the modified zinc anodes was characterized using AFM and scanning electron microscopy (SEM) (Phenom ProX, Netherlands), operating at an accelerated voltage of 15 kV. The chemical compositions were determined through X-ray photoelectron spectroscopy (XPS) (K-α XPS, Thermo Scientific). The spectrum was charge shifted by fitting with the standard of the C 1s peak at 284.8 eV. Grazing incidence wide-angle X-ray scattering (GIWAXS) measurements were conducted at the Canadian Light Source (CLS),[25] employing X-rays with a wavelength of $\lambda = 1.25916$ Å. The beam was directed onto the surfaces at grazing incidence angles of 0.15°, with a sample-to-detector distance of 173 mm. Each sample was exposed for 5 seconds. An LaB_6 calibrant standard was measured to correct for beam offset and tilt, with calibration and azimuthal integration performed using the GSAS-II software suite.[26] Azimuthal integration was calibrated using GSAS-II software.

2.4 Electrochemical measurement

A symmetric configuration in Pyrex glass cells was constructed with 1 cm × 1 cm anodes as the working electrode (immersed by 0.5 cm^2) for chronoamperometry and linear sweep voltammetry measurements. For both the symmetric cells and full cells, CR2032-type coin cells were assembled with a 19 mm diameter glass fiber separator, a 16 mm diameter zinc disk (0.01" in thickness), and 3 M $ZnSO_4$ electrolyte under ambient conditions. For the V_2O_5 full cells, V_2O_5 slurry coated stainless foil was punched to a slightly smaller size (14 mm) than the anodes, having 4.3 mg cm^{-2} of active material loading mass. Galvanostatic charge–discharge measurements were carried out under different conditions on a NEWARE multichannel battery cycler. Chronoamperometry and impedance spectroscopy were carried out using a potentiostat (VSP-300, BioLogics). For the hydrogen evolution reaction (HER) test, Zn anodes were used as working electrodes, Ag/AgCl (in 3 M saturated KCl) as the reference electrode, and platinum (Pt) wire as the counter electrode in N_2 purged 1 M Na_2SO_4 electrolyte. Additionally, the backside of each sample was sealed with Kapton chemical resistive tapes to prevent the spontaneous reaction at the non-treated or non-deposited surface. Distribution of relaxation time (DRT) analysis was performed using DRTtools[27] to present the impedance as a function of relaxation time constant. To avoid overestimation of artificial peaks, a regularization parameter of 10^{-2} was chosen.

2.5 Finite element simulation

The two-dimensional finite element method simulations were conducted using COMSOL Multiphysics, employing the "Electrodeposition Tertiary Current Distribution, Nernst–Planck" model. The migration of the electrolyte was governed by the Nernst–Planck equation, while the electrode reactions at the electrodes followed the Butler–Volmer equation. The concentration field distribution at the anode and electrolyte surfaces was simplified in two-dimensional (2D) constructions with a narrow range of 2 × 2 μm, based on AFM images. The particle size and geometry of the simulated nanoparticles were set to emulate that observed from the AFM image in Fig. 3 of the main manuscript. The overall interparticle spacing used between particles was established through image analysis using disLocate[28] and GISAXS diffraction pattern analysis shown in SI Fig. S1. The inherently rough surface of the Zn anode was constructed using three protrusions with a height of 50 nm, roughly mimicking the bare Zn foil electrode surface observed in the AFM micrographs in SI Fig. S2. The applied potential for electrodeposition was set to −150 mV, with an initial Zn^{2+} concentration of 3 M. The diffusion coefficient of Zn^{2+} species in the electrolyte was set to $3.3 \times 10^{-10}\ m^2\ s^{-1}$. The current density for electrodeposition in the cell was set at 5 mA cm^{-2}. The entire surface at the bottom was modeled as pure Zn with a conductivity of $1.69 \times 10^7\ S\ m^{-1}$, while the spherical gold particles were set as current conductors with a conductivity of $4.1 \times 10^7\ S\ m^{-1}$.

2.6 DFT calculation

DFT calculations were performed using GPAW 22.8.0, a Python-based code that utilizes the projector-augmented wave (PAW) method.[29] The Revised Perdew–Burke–Ernzerhof (RPBE) exchange–correlation functional was employed.[30] Ionic cores were represented by pseudopotentials derived from the PAW approach, as provided in the GPAW package.[31] The bulk structures were optimized to calculate lattice parameters using a plane-wave energy cutoff of 800 eV. The Brillouin zone was sampled using 8 × 8 × 8 Monkhorst–Pack k-point grids. Structural optimizations were considered converged when the maximum force on any atom was less than 0.05 eV $Å^{-1}$. To facilitate self-consistent field (SCF) convergence, the occupation of Kohn–Sham eigenstates was smeared with a Fermi–Dirac distribution of 0.1 eV for metallic systems. All calculated energies were extrapolated to $k_{TB} = 0$ eV.

Two types of surface slabs were optimized to compare bare Zn surfaces and Zn surfaces with assembled Au nanoparticles. For the bare Zn surface, Zn(002) slabs were modeled using periodically repeated (2 × 2) four-layer supercells derived from the optimized bulk structure. To represent Au NP decorated Zn surfaces, a cluster of five Au atoms, representing an Au(111) surface, was first optimized in vacuum and then deposited on a (4 × 4) Zn(002) surface with the sequential structural optimization of the Au cluster on the Zn surface. This configuration described an isolated Au nano-cluster periodically deposited on a Zn surface. Periodic boundary conditions were applied, with a 15 Å vacuum layer introduced perpendicular to the surface to prevent interactions between periodic images. During structural optimizations, only the topmost layer and adsorbates were allowed to relax, while the bottom layers were constrained to their bulk positions. Both surface optimizations and density of states (DOS) calculations were performed using a plane-wave energy cutoff of 500 eV and a 3 × 3 × 1 Monkhorst–Pack k-point grid. Structural optimizations were also converged when the maximum force on any movable atom in any direction was less than 0.05 eV $Å^{-1}$. The adsorption energy was calculated from:

$$E_{\text{ads}} = E_{\text{total}} - E_{\text{slab}} - E_{\text{adsorbate}} \tag{1}$$

where E_{ads} is the adsorption energy, E_{total} is the total energy of the slab and adsorbate, E_{slab} is the total energy of the slab and $E_{\text{adsorbate}}$ is the energy of the adsorbate. The climbing image nudged elastic band (CI-NEB) calculations were performed to calculate the diffusion energy barriers along the x-axis and diagonal pathway from the most stable adsorption site with five images and the tangential force convergence criteria of 0.05 eV $Å^{-1}$ (ref. 32).

3 Results and discussion

Typically, Zn surfaces are prone to dendritic formation due to surface protrusions and imperfections which act as nucleation sites, as shown in the schematic in Fig. 1. Using finite element simulation conducted with COMSOL Multiphysics, we illustrate this effect in Fig. 1(a).

The inherently rough surface of the Zn anode was constructed using three protrusions, roughly mimicking the observed bare Zn foil electrode surface (see the AFM micrographs in SI Fig. S2). The simulation shows that the Zn^{2+} species are concentrated in protruding areas where the charges are accumulated, a behaviour commonly referred to as the 'tip effect'.[6] This causes an irregular concentration field of cations, as well as preferential diffusion of Zn ions to the protrusions, resulting in inhomogeneous nucleations that grow into severe dendrites as illustrated schematically in Fig. 1(b). Conversely, a similar simulation with the proposed introduction of sparse Au NPs on a Zn surface (Fig. 1(c)) yields a homogeneous ionic flux of Zn cations due to the highly conductive nature of the gold substances compared to Zn.

As depicted schematically in Fig. 1(d), the concentration of Zn species is evenly distributed as the conductive Au NPs are able to compensate for the uneven electric field distribution caused by the rough surface protrusions. This results in the formation of numerous nucleation sites regardless of the

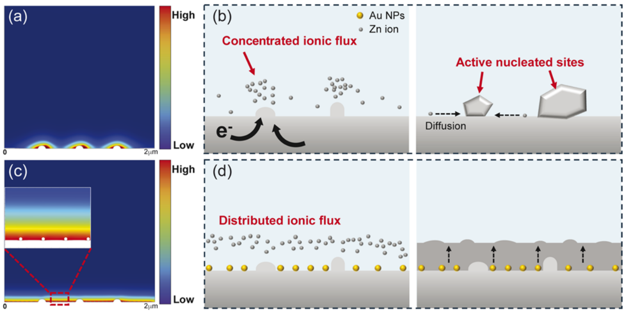

Fig. 1 Simulated models of the initial concentration field distribution of Zn^{2+} species and schematic illustration of the Zn plating process on the (a and b) bare Zn and (c and d) Au NPs deposited on Zn, respectively.

presence of surface defects, encouraging uniform film plating with 3D diffusion of Zn ions.

DFT calculations were further performed to investigate the adsorption and diffusion properties caused by isolated Au NPs on a Zn surface. Initially, an Au cluster consisting of 19 atoms, representing the (111) surface, was optimized in a vacuum. Subsequently, a smaller Au cluster with five atoms was deposited onto a 4 × 4 Zn(002) supercell to avoid the interactions between periodically repeated Au clusters.

Au is already a known zincophilic material, as confirmed by DFT calculations conducted by Ren *et al.*[14] comparing the adsorption properties on pure Zn with Au surfaces. However, the calculated projected DOS in Fig. S3 indicates that the d-states of the Au cluster were modified compared to the pure Au(111) surface. Specifically, the d-band center was positively shifted by 0.062 eV, and the bandwidth was also broadened. These adjustments suggest that the Au NP cluster may exhibit stronger electronic interactions with Zn adsorbates, by showing increased band overlap with the d-band of Zn adsorbate and a upshift of the d-band to the Fermi level, compared to the pure Au(111) surface.[33] Here, therefore, we highlight the influence of sparse clustered Au on the Zn surface, rather than full coverage. The adsorption energies were calculated for both a bare Zn surface and a Zn surface with an Au cluster, which are periodically repeated. All possible adsorption sites, considering their symmetry, were examined as shown in Fig. S4.

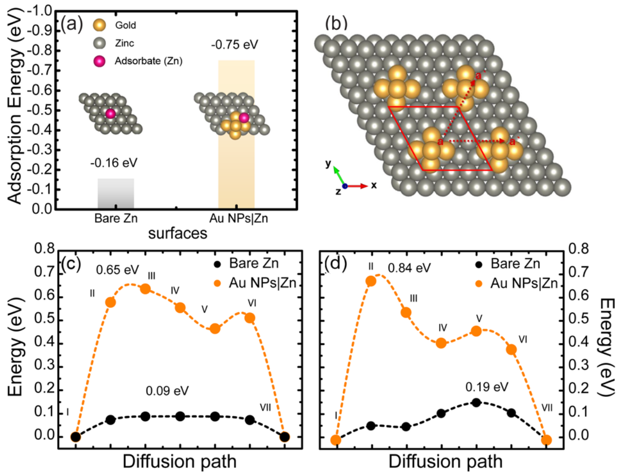

Fig. 2 (a) The adsorption energy of Zn adsorbate on the surface of bare Zn and Au NPs|Zn (the inset represents the corresponding adsorption sites). (b) Schematic of Zn atom diffusion along the *x*-axis and diagonal pathway on the Au NPs|Zn slab. (c and d) The calculated energy difference profiles on both bare Zn and Au NPs|Zn.

As illustrated in Fig. 2(a), the Zn surface combined with an Au cluster emerges as the favorable nucleation site by exhibiting significantly lower adsorption energy compared to the lowest adsorption energy on the bare Zn surface. The lowest adsorption energy in the presence of the Au cluster was nearly five times greater than that on the bare Zn surface, highlighting the enhanced zincophilicity. This indicates that the uniformly dispersed Au NPs can act as effective nucleation sites, possibly lowering nucleation barriers and improving surface kinetics.[34] Bader charge analysis provides further evidence, revealing stronger charge transfer between the Au cluster and Zn adsorbate, with approximately $0.27e^-$ transferred. In contrast, only $0.04e^-$ was transferred between the Zn adsorbate and the bare Zn surface. This trend is depicted in Fig. S5 through charge density difference mapping, which shows charge accumulation (yellow regions) at the interface between the Zn adsorbate and the adsorption site on the edge of the Au cluster, alongside greater charge depletion (cyan regions) around the adsorbate exterior comparing with the charge distribution of the Zn adsorbate and Zn surface.

The relative energy differences among seven adjacent adsorption sites along both the *x*-axis and diagonal diffusion pathways were additionally calculated, starting from the most favorable adsorption site, as illustrated in Fig. 2(b). Fig. 2(c) and (d) reveal diffusion energy barriers of 0.09 eV and 0.19 eV on the bare Zn surface, compared to significantly higher barriers of 0.65 eV and 0.84 eV with the introduction of the Au cluster for the *x*-axis and diagonal pathways, respectively. These results indicate that the bare Zn slab is more prone to the occurrence of 2D migration of Zn adatoms, accelerating uneven nucleation at specific locations, while the presence of homogeneously distributed Au NPs constrains the 2D diffusion of Zn atoms.[17] This constraint effectively prevents the formation of inhomogeneous aggregations, which could otherwise grow extremely large during continuous plating.

To confirm the proposed mechanism, Au NPs were deposited on Zn foil surfaces, with particle size and spacing deliberately chosen to be smaller than the RMS roughness of the Zn anode (∼13 nm, see SI Fig. S2). High-resolution SEM micrographs (Fig. 3(a)) directly confirm the presence of isolated Au NPs on the Zn foil, showing uniform dispersion across the surface without evidence of aggregation. Owing to the intrinsic roughness of the Zn foil, however, quantitative determination of nanoparticle size and interparticle spacing by AFM is not reliable on Zn substrates.

To enable accurate statistical analysis, identical Au NP arrays were therefore deposited on atomically flat Si wafers under the same reverse micelle deposition and plasma-removal conditions (Fig. 3). With an average size of ∼5 nm, extracted from the Gaussian distribution of particle heights shown in Fig. 3(c), the nanoparticles form a sparse submonolayer array of uniform

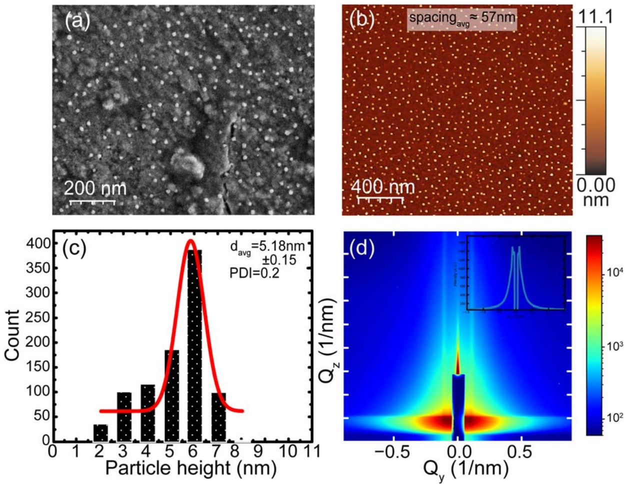

Fig. 3 (a) High resolution SEM micrograph of dispersed Au NPs on Zn foil; (b) AFM micrograph of dispersed Au NPs on a Si wafer; (c) height distribution of particles with a Gaussian distribution curve; (d) GiSAXS pattern of Au NP arrays on Si wafer. Inset of the line profile at Q_z showing the interparticle spacing for Au NPs on Si.

particles that do not completely cover the underlying surface. The interparticle spacing is ∼60 nm, as determined independently by spatial statistical analysis of the images using disLocate[35] and by GiSAXS analysis of the deposited particles (see SI Fig. S1).

One of the key advantages of reverse micelle templating is the reproducibility of nanoparticle size and spacing across chemically and topographically distinct substrates, as demonstrated by comparative AFM images on multiple surfaces (see SI Fig. S6). The SEM confirmation on Zn foil, combined with quantitative AFM and GISAXS analysis on Si, therefore establishes that the Au NP arrays on Zn possess the same sparse, isolated geometry used in subsequent electrochemical and modeling studies.

In Fig. 4(a), chronoamperometry experiments of bare Zn foil, Au NPs|Zn, and plasma treated Zn (O_2PT|Zn) were performed at an overpotential of −150 mV to analyze surface diffusion kinetics in a beaker cell without a separator. Plasma treated surfaces were included, both as plasma treatment has been previously shown to improve the performance of Zn electrodes,[36] and because an O_2 plasma etching step is necessary in the formation of Au NPs by reverse micelle templating. For bare Zn, the current density gradually decreases for the initial 90 seconds, indicating dominance by 2D diffusion. Zinc ions are absorbed onto the restricted active spots of bare Zn and migrate along the surface to favorable sites for plating, which are at random defects and surface protrusions, due to the low diffusion barrier found in the DFT calculations. Essentially, this is a consequence of the uneven electric field distribution shown in the finite element simulation, driving accumulation of adsorbed ions at the tips to form large nucleation sites.[37,38] This uneven initial aggregation further amplifies the local electric field near the tips, leading to severe dendritic growth. Such behaviour was observed by SEM (see Fig. 4(c)) after a 3 min plating step. In contrast, Au NPs|Zn and O_2PT|Zn anodes quickly achieved relatively constant current densities, which indicates the 3D diffusion of Zn ions along the vertical direction, after only a few seconds of the 2D diffusion process as the Au NPs effectively constrained the migration of Zn adatoms as confirmed by DFT calculations. These transitions from 2D to 3D behaviour are shown by the dotted vertical lines in Fig. 4(a). Additionally, the larger absolute magnitude of initial current densities for the treated surfaces compared to bare Zn supports the concept of a higher density of nucleation sites for both plasma processing and the incorporation of the Au NPs. The magnitude of the initial current densities is a reflection of the active surface area with abundant sites attractive to zinc cations, which immediately undergo reduction, thereby creating numerous nucleation sites.[16] The distribution of nucleation contributes to the suppression of densely aggregated formations, as suggested by the simulation in Fig. 1. Noticeably, Au NPs|Zn produces a more negative current density at the initial plating compared to the O_2PT|Zn cell, suggesting that the Au NPs themselves contribute significantly to generating more active nucleation active sites by attracting Zn^{2+} ions to the low charged areas. This is consistent with the work of Ren *et al.*[14] who showed the high zincophilicity of Au aiding in Zn plating, possibly due to the superior electrical conductivity of Au.[39]

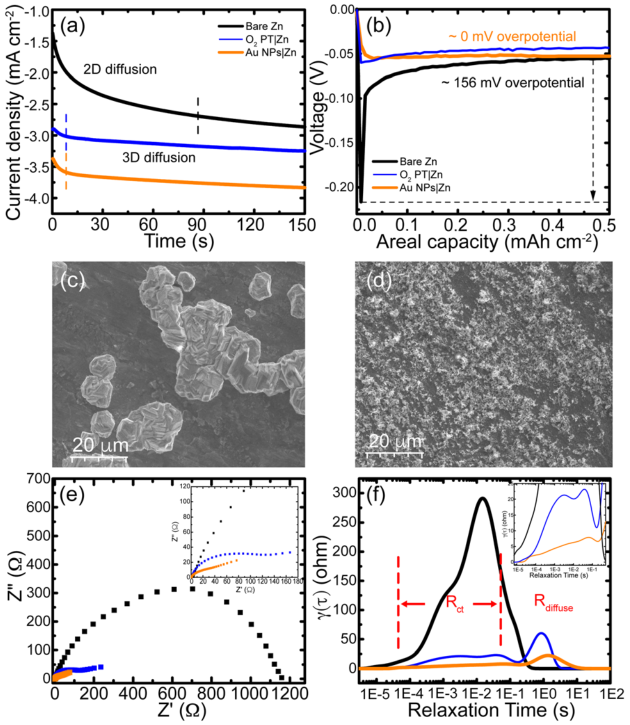

Fig. 4 (a) Chronoamperometry of symmetric configurations at −150 mV (the vertical dotted line denotes the transition point from 2D to 3D diffusion), (b) nucleation overpotential at 1.0 mA cm^{-2} with the capacity of 1 mAh cm^{-2}. SEM micrographs after 3 min deposition at −150 mV on (c) bare Zn and (d) Au NPs|Zn. (e) Nyquist plots and (f) DRT profiles converted by EIS with the insets showing the regions of lower impedance area and relaxation time, respectively.

The chronoamperometric behavior of CR 2032 symmetric coin cells with a glass fiber separator, shown in Fig. S7, confirms the general tendency observed for the electrode surfaces. The Au

NPs|Zn cell showed the smallest difference between the initial and final current density after plating for 10 minutes, as well as a larger absolute magnitude of initial current density, suggesting that the submonolayer array of Au is the most effective way to suppress the dendritic behavior, regardless of cell type.

The reduced barrier to nucleation for the Au NPs|Zn surface is also shown experimentally by the initial nucleation overpotential observed during the galvanostatic discharging process for symmetric coin cells shown in Fig. 4(b). Such barriers, which control subsequent plating behaviour, are determined by the deviation in values between the initial highest potential and its plateau overpotential.[40,41] At 1 mA cm^{-2}, the bare Zn cell required a high overpotential of 156 mV to overcome the initial nucleation energy barrier, likely due to the lower surface energy compared to both O_2PT|Zn and Au NPs|Zn surfaces, as well as the inferior quality of the uneven native oxide layer on the bare surface,[40] ultimately leading to the severe agglomeration observed. By contrast, the initial nucleation potential of Au NPs|Zn was nearly 0 mV as evidenced by the flat voltage profile. Some of the enhanced nucleation was clearly due to the plasma treatment as a reduced overpotential of 19 mV was observed in the O_2PT|Zn cell. Both instances indicate a favorable condition for homogeneous plating across the surface, although the plateau overpotential (surface overpotential) of the O_2PT|Zn cell is slightly higher than that of Au NPs|Zn. Tafel curves using a 3 M $ZnSO_4$ electrolyte (SI Fig. S8) shows a slightly higher exchange current density of Au NPs|Zn than bare or O_2PT|Zn suggesting that the electron charge transfer at the electrode/electrolyte surface is more favorable, which should lead to higher zinc deposition on the Au NPs|Zn surface.

This enhanced homogeneous plating is visible when comparing the SEM micrographs after 3 minutes plating at −150 mV overpotential in Fig. 4(c) and (d) where the Au NPs|Zn electrode obviously shows smoother, more uniform Zn coverage with distributed nucleation, compared to the numerous large agglomerated Zn plates with sharp vertexes on bare Zn. In SI Fig. S9, the SEM micrographs obtained after galvanostatic plating at 5 mA cm^{-2} for 1 hour in a beaker cell without a separator also clearly display the homogeneous and smooth plating on Au NPs|Zn electrodes, whereas severely sharpened dendrite growth and their uneven aggregation occurred on bare Zn. The Au NPs do not appear to favour a particular growth direction, as the geometric shape of the plated layers are similar to each other for O_2PT|Zn and Au NPs|Zn. This is supported by a GiWAXS analysis of the deposited Au NPs (see SI Fig. S10) showing randomly distributed orientational order in powder rings with no specific texture. However, the Au NPs|Zn surface seems to exhibit a larger activated surface area for nucleation, given that the coverage rate of the deposited Zn layer is typically over 70%, compared to ∼45% for the O_2PT|Zn surface, as depicted in SI Fig. S11. This trend also corresponds to the chronoamperometry results discussed above.

To examine the potential for undesirable side reactions, the hydrogen evolution reaction (HER) on various surfaces was examined. In general, Au is not considered an active catalyst for the HER, but can often be activated when coupled with other materials.[42] The deposition of an ultra-low sparse amount of Au NPs on the Zn surface slightly suppresses HER activity compared to bare Zn, as evidenced by the negatively shifted potential to reach 10 mA cm^{-2} as shown in Fig. S12(a). Although Au NPs themselves may act as catalysts for the HER, as shown in Fig. S12(b) where Au NPs were investigated on a non-catalytic Si wafer, their catalytic activity toward the HER was significantly lower than that of the Zn surface, resulting in the lowered overall HER activity of the Au NP|Zn surface. In contrast, the cathodic plots for various substrates reveal that the O_2PT|Zn substrate undergoes an enhanced HER, achieving a current density of 10 mA cm^{-2}, at a potential of only −1.471 V. This result surpasses that of both bare Zn and Au NP|Zn electrodes, likely due to the improved hydrophilicity of the Zn surface by plasma treatment.[43] The enhanced hydrophilicity, confirmed by the contact angle measurements in Fig. S13, implies an increased number of active sites for water molecules.

Notably, though the Au NP|Zn surface demonstrated a lower contact angle than the O_2PT|Zn surface alone as shown in Fig. S13, its HER activity was significantly suppressed compared to the O_2PT|Zn surface. This indicates that the sparse array of Au nanoparticles can overcome the enhanced hydrophilicity from plasma etching, probably due to the intense binding interactions between hydrogen and Au atoms.

Corrosion reactions are also undesirable at electrode interfaces, as they can form dead spots on the Zn surface that no longer contribute to the cycling. In addition to the Tafel curves (SI Fig. S8) showing a positively shifted corrosion potential compared to the untreated Zn anode, indicating suppressed corrosion despite the sparse coverage of Au,[44,45] electrochemical impedance spectroscopy (EIS) analysis of symmetric cells assembled using a 3 M $ZnSO_4$ electrolyte suggests that the performance within a battery structure will be enhanced with the Au NPs|Zn composite surface. The real part intercept at the high-frequency region of the Nyquist curves, Fig. 4(e), shows higher intrinsic resistance of both the electrolyte and electrode, suggesting that the resistance at the electrode with Au NPs is reduced.[46] Moreover, both real and imaginary values in the intermediate frequency range are significantly lower for the Au NPs|Zn anode compared to the others, suggesting faster charge transfer kinetics at the interface.[46] As a more reliable approach to distinguish the interfacial electrochemical processes at the electrode interface,[47,48] distribution of relaxation time (DRT) analysis was performed using DRTtools[27] to present the impedance as a function of relaxation time constant, as depicted in Fig. 4(f). This allows the deconvolution of the independent interfacial electrochemical kinetics based on the time constant determined by the transition of charges.

Among the spectra, the Au NPs coated Zn anode exhibits the lowest impedance magnitude across varying time constants, particularly in the intermediate constant time range from 0.1 ms to 63 ms, which is attributed to the interfacial charge transfer process (R_{ct}), including the zinc nucleation.[49] In contrast, consistent with the Nyquist plot of EIS, R_{ct} values of both bare Zn and O_2PT|Zn are higher than that of Au NPs|Zn electrodes. Interestingly, both bare Zn and O_2PT|Zn possess additional peaks below the main R_{ct} peak of zinc nucleation, suggesting sluggish kinetics at the interface due to undesirable side reactions[50,51] (likely the HER at the O_2PT|Zn, and corrosion at the Zn surface). These are completely suppressed on the Au NPs|Zn surface.

From another perspective, the features observed between 10^{-5} and 10^{-3} s represent the interfacial migration of Zn ions prior to the onset of charge transfer, as detected in both bare Zn and O_2PT|Zn.[52] The significant suppression of this migration-related response in the sparse Au NP decorated electrode corresponds to the constrained migration due to the uniformly dispersed, highly zincophilic Au NPs that provide abundant and favorable nucleation sites. This effectively constrains lateral ion migration at the interface, suppressing 2D growth as seen in the chronoamperometry, resulting in a negligible migration peak compared with the counterparts. Furthermore, a higher ion-diffusion resistance was observed on the surface of O_2PT|Zn compared to the Au NPs|Zn at the largest time constants, implying the presence of an undesirable barrier layer disrupting the diffusion of Zn^{2+} to the nucleation active sites.[39]

This was supported by an XPS analysis of the various electrode surfaces. Both synchrotron GIWAXS profile (Fig. 5(a)) and high resolution XPS core level spectra (Fig. 5(c)) confirm the presence of crystalline metallic Au after removal of the polymer micelles. At an incident angle of 0.15 with 1.25916 Å wavelength X-rays, GIWAXS for Au NPs deposited on Si shows the distinct (111) and (200) diffraction peaks at q = 2.68 Å and 3.09 Å respectively, corresponding to metallic Au particles,[53] randomly oriented on the surface (see SI Fig. S10). Similarly, as shown in Fig. 5(c), the Au 4f core level XPS spectra show the expected metallic Au $4f_{7/2}$ and Au $4f_{5/2}$ binding energy peaks at 84.2 and 87.9 eV with peak splitting of 3.7 eV.[54,55] There are small features at around 90 eV and 87 eV that correspond to unreacted complexed $AuCl_4$ (ref. 56 and 57) or Au sub-oxides.[55] As the Zn 3p region overlaps with the Au 4f region, the XPS spectra of the Au NPs|Zn confirm the co-existence of anchored Au NPs on the Zn foil surface, as shown in Fig. 5(c). Both Zn 3p and Au 4f spectra can also be deconvoluted using Gaussian peak fitting, revealing four distinct peaks at 83.1 eV and 86.8 eV for Au $4f_{7/2}$ and Au $4f_{5/2}$, and 88.6 eV and 91.3 eV for Zn $3p_{3/2}$ and Zn $3p_{1/2}$, respectively. Though $AuCl_4$–carbon complexes have been observed with 4f spectra near these regions,[56,57] the bare Zn surface clearly shows the coincident position in the Zn 3p spectra.

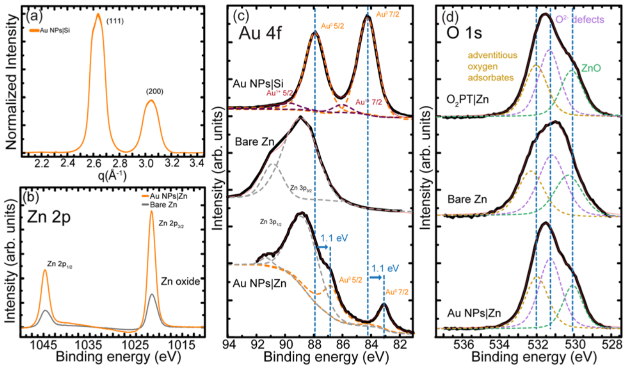

Fig. 5 Characteristics of the bare Zn and Au NPs|Zn electrodes: (a) the integrated 1D powder diffraction of GiWAXS; (b–d) high resolution XPS core level spectrum of (b) Zn 2p of bare Zn and Au NPs|Zn, (c) Au 4f region which includes Zn 3p of Au NPs|Si and Au NPs|Zn. The bare Zn is extracted from the low resolution survey scan of the same region. (d) O 1s of bare Zn, plasma treated O_2PT|Zn, and Au NPs|Zn.

Interestingly, there is also a clear negative peak shift of 1.1 eV in the binding energy of the Au $4f_{7/2}$ peak compared to Au NPs on a Si wafer. The Bader charge analysis showed an overall $0.25e^-$ of transferred charge from the Zn slab to the Au cluster, possibly due to the different electronegativity of Au and Zn, corresponding to the negative peak shift in the XPS spectrum. It is likely that this is combined with an electron transfer between Au and oxygen vacancies in the native or simultaneously formed oxide on the Zn surface during the plasma etching.[58,59] However, no detectable peak shift was observed in the Zn 2p or 3p spectra, corresponding to ZnO, between substrates with and without Au NPs shown in Fig. 5(b) and (c), which may be due to a dominant signal from the substrate Zn foil. The interaction between Au and Zn or ZnO suggests the formation of a heterostructure at the contact surface, which enhances the electronic contact as well as the adhesion between Au NPs and the Zn surface. It is likely that the heterostructure induces a charge density redistribution along the dispersed interfaces of Au NPs and Zn surfaces, contributing to the enhanced zincophilicity around the Au NPs acting as designated nucleation sites.

High-resolution O 1s spectra indicate the formation of a high-quality ZnO passivation layer for both plasma treated and Au decorated Zn foil, which supports the reduced nucleation overpotential observed in Fig. 4(d).[36,60] Previous studies have also shown increased uniformity of Zn deposition using artificially produced high quality ZnO layers.[61,62] Fig. 5(d) shows that the oxygen species present on O_2PT|Zn and Au NPs|Zn surfaces are mostly the same but distinct from the untreated bare Zn surface, suggesting that they result from the plasma treatment step. A Zn–O binding peak at 530 eV corresponding to fully oxidized ZnO is observed on all surfaces;[36,63] however, the peaks from O_2PT|Zn and Au NPs|Zn are more pronounced than those from bare Zn, with a slight shift towards lower binding energy. This suggests that the plasma removes some of the adventitious oxygen adsorbates on the surface, which can promote homogeneous Zn plating. Therefore, unlike the native oxidation that occurs under ambient exposure, plasma treatment produces uniform ZnO at the interface, which improves Zn plating. In addition, there is also an increase in oxygen-deficient species in the matrix of ZnO,[36,63] providing abundant sites for the observed charge transfer to the Au NPs.

Our study has revealed that a periodically structured sparse Au array introduces long-range charge transport enhancement, reducing local overpotentials, suppressing side reactions and promoting uniform electroplating, suggesting highly efficient and stable interlayer for Zn electrodes. To evaluate the galvanostatic charge–discharge performance of Au NP decorated Zn anodes, symmetric cells were tested under various constant current densities and capacities. To test the enhancement capabilities of the Au decorated array, we chose a high concentration (3 M) of $ZnSO_4$, resulting in an aggressive environment where the cell was compromised quickly resulting from the poor wettability of the separator.[64]

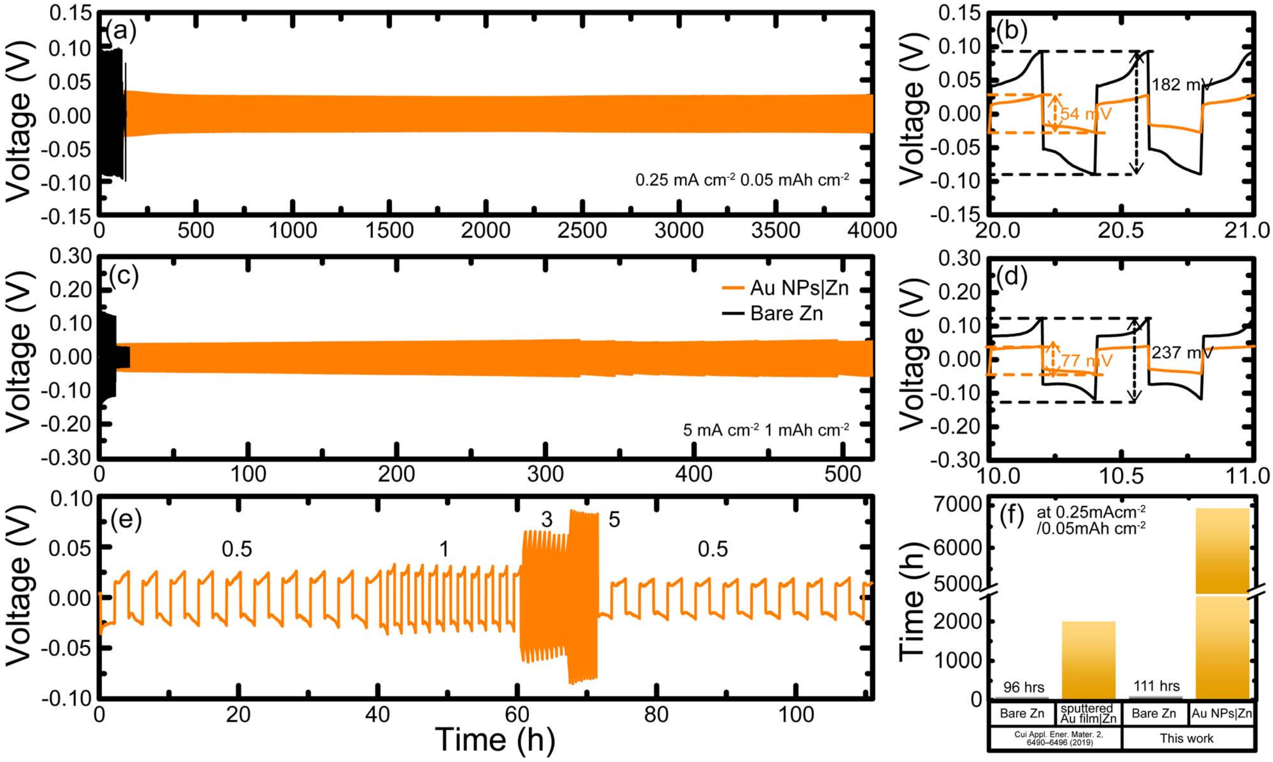

Fig. 6 Galvanostatic charge/discharge tests of symmetric cells (a and b) at 0.25 mA cm^{-2} and 0.05 mAh cm^{-2}, and (c and d) at 5 mA cm^{-2} and 1 mAh cm^{-2}, respectively. (e) The rate performance of the symmetric battery (at 1 mAh cm^{-2}) and (f) the cycling performance compared to the sputtered Au protective layer on Zn anodes under the same test conditions.

The cycling performance of the cell with the bare Zn showed an internal short-circuit after 118 h at 0.25 mA cm^{-2} shown in Fig. 6(a), caused by severe dendrite formations. In contrast, the cell incorporating the Au NPs|Zn maintains ultra-long cycle stability, lasting well beyond 4000 h (as shown) with uniform voltage hysteresis, with eventual short circuit occurring only after 6962 h. Additionally, in Fig. 6(b) the voltage hysteresis of the bare Zn cell is more than three times higher than the Au NPs|Zn cell (54 mV). The lower hysteresis for the decorated electrodes is maintained consistently for the entire operation. This reflects a highly active and stable operation of the Au NPs|Zn anode.[65,66] As the particle size can be easily tuned with RMD (see SI Fig. S14), we also tried larger Au NPs decorated on Zn foil under the same measurement conditions. They also exhibited similar enhanced cycling performance to the smaller Au NPs. However, its voltage profile fluctuated more during cycling, particularly after 1000 h as shown in SI Fig. S15. This is likely a result of the higher surface coverage and more disordered size and array of Au NPs, which can lead to longer and inhomogeneous diffusion pathways of the Zn ion locally at the top surface of the NPs. Similarly, Kim *et al.* observed that a smaller curvature of seed micro-arrays showed better morphology during electrodeposition.[67]

The impact of a sparse array of Au NPs on the plating/stripping performance was also tested at 5 mA cm^{-2} as depicted in Fig. 6(c). Again, enhanced stability and lowered hysteresis (Fig. 6(d)) of the symmetric cell with an Au NP modified Zn anode was observed, lasting for 530 hours, compared to the bare Zn cell, which failed after only 11 hours. Severe dendrite formation, which pierced the separator, can be seen in SI Fig. S16.

Under these conditions, plasma-treated Zn electrodes were also tested to separate the impact of plasma treatment from that of the Au decoration (SI Fig. S17). The O$_2$PT|Zn electrode exhibits enhanced cycling performance compared to the bare Zn foil, with 202 hours lifetime with reduced hysteresis. SI Fig. S16(c) of the disassembled cells shows significantly less dendritic growth, and fewer attached fibers from the separator. This enhancement by oxygen plasma treatment has been previously demonstrated,[36] and attributed to the elimination of naturally absorbed chemical species as well as the formation of high-quality of the ZnO layer,[60] which we also observed from our XPS results. However, the voltage hysteresis was higher than for the Au NPs|Zn, and around 186 hours started to increase and abruptly fluctuated with intense magnitude. This behaviour suggests the formation of an insulating layer possibly induced by precipitated dead Zn due to insufficient conductivity of the oxide layer without Au NPs.

It is also likely that the enhanced HER activity at the O$_2$PT|Zn electrode surface promoted the generation of micro-bubbles at the interface, resulting in the formation of dead Zn and current inefficiency that are detrimental to the cycling performance. By contrast, the Au decorated film showed much smaller dendrites (SI Fig. S16(d)) and a high uniformity over the surface.

The high stability of the Au NPs|Zn surface is also shown in Fig. 6(e), where the cell was cycled under increasingly harsh conditions, then returned to 0.5 mA cm^{-2} with almost no loss of performance.

Moreover, galvanostatic cycling performances at higher capacities were also conducted as shown in Fig. S18. At 3 mA cm^{-2} and 1.5 mA cm^{-2}, the cell assembled with Au NP| Zn again presents much longer stability with stable voltage hysteresis compared to the bare Zn. Even at intensively high current density and capacity (10 mA cm^{-2} and 10 mAh cm^{-2}) the sparse NP decoration increases the cycling lifetime. This demonstrates the effectiveness of Au NP decoration on the Zn surface to increase cyclability compared to the bare Zn anode under all conditions.

Table 1 summarizes various state-of-the-art interfacial layers used on Zn anodes and their relative improvements in cycles to short circuit lifetimes. To ensure a fair comparison, the best cycling performances measured under similar current densities and areal capacities to the devices in this study are considered, as the cyclability of symmetric cells strongly depends on operating conditions. Furthermore, the table describes the relative increase in lifetime from the performance of the reported bare Zn anodes to ensure comparability as other experimental parameters such as electrolyte salt type and concentration,[64] separator thickness, pore size and wettability,[68] and cell pressure also practically influence cell performance. Details of the cycle life and structure are provided in SI Table S1. As shown in Table 1, a variety of interlayer materials have been introduced to improve the stability of the Zn anode, and most strategies and materials on the anode surface result in enhanced cycling performances compared to the bare anodes.

Particularly, compared to previous studies on the cycling performance of symmetric cells with sputtered Au interphase films, the sparse coverage of our Au NPs appears to play a significant role in improving the cycling stability. As shown in Fig. 7(f), symmetric cells with Au NPs|Zn electrodes measured at 0.25 mA cm^{-2} last at least 58 times longer than bare Zn, while the cell with sputtered Au nanolayers (~100 nm) from Cui *et al.*[13] had only around 22 times enhanced stability, measured at the same electrolyte concentration. It also showed enhanced relative stability, with over 45 times improvement in the cycling lifetime compared to thinner sputtered layers with other electrolyte concentrations at 5 mA cm^{-2} as also summarized in Table 1 and Fig. 7. The sparse submonolayer nature of the Au NP array, with extremely low Au density and stronger electronic interactions with Zn (as indicated by the DFT calculations in SI Fig. S3) compared to sputtered monolayers significantly enhances cycling performance due to its unique geometry. Uniformly isolated Au NPs that restrict the migration of Zn adatoms, and increased band overlap with the d-band of Zn adsorbate differ fundamentally from both densely coated and unstructured nanoparticle surfaces, suggesting that charge dynamics are tuned through periodic spatial modulation. These sparse Au particles also outperform alternative strategies such as larger microparticles, doping, or CVD-deposited interlayers with other materials, delivering nearly an order of magnitude improvement in cycling lifetimes (Table 1). Only sputtered Fe films exhibited greater absolute improvements, but these require high-vacuum batch processing,[72] in contrast to the simple, solution-based approach of our nanoparticle arrays, which is compatible with scalable roll-to-roll manufacturing.

Though Au is a precious metal, with costs of roughly \$65 per g (USD),[73] scaling down to nanoparticle decoration leads to

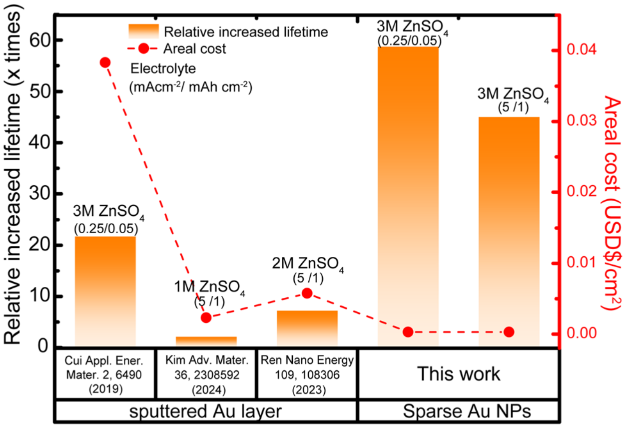

Fig. 7 Relative cycling enhancements of Zn anodes achieved by sparse Au nanoparticle arrays compared to fully sputtered Au interlayers, highlighting performance gains alongside cost effectiveness.

Table 1 Summary of surface engineering strategies for Zn anodes and their corresponding lifetime improvements in symmetric cells

Materials	Methods	Cycling enhancement (×)[a]	Conditions[b]	Ref.
Au	NPs	~58.7	0.25/0.05	This work
		~45	5/1	
Au	Sputtered	~2.2	5/1	15
Au	Sputtered	~7.2	5/1	14
Au	Sputtered	~21.7	0.25/0.05	13
		~8.2	5/2	
Sn	CVD film	~4.5	1/0.5	69
Si	NPs	~5.6	5/1	70
CuO@C	Particles	~9.5	1/1	34
Cu	Doping	~12.6	0.5/0.5	17
Ag	Pasted film	~15.7	1/1	71
Fe	Sputtered	~100	1/0.5	72

[a] Improvements relative to the performance of bare Zn anodes. [b] Applied current density/areal capacity (mA cm^{-2}/mAh cm^{-2}).

significant cost savings as shown in Fig. 7. For coin cells with 2 cm^{-2} electrode area, the cost at lab scale is roughly $0.000283 per cm^2 (see the SI). This is an order of magnitude cheaper than the $0.0023 per cm^2 for a sputtered Au layer as described by Kim *et al.*[15] and the other thicker sputtered Au film studies as highlighted in Fig. 7. Using the performance of our full cells, the total bulk material cost for the electrodes would be as low as $33 per kWh, without considering any economies of scale reducing the precursor costs. This is less than half of the $65 per kWh proposed for state of the art low cost ZIB batteries,[74] and even cheaper than the best proposed market scenario for lithium ion battery (LiB) technologies by 2030 ($48.6 per kWh).[75]

Finally, full-cells were assembled with commercial V_2O_5 cathodes to confirm the effectiveness of sparse Au NPs in practical battery applications. We utilized industrially processed V_2O_5 slurry coated on stainless steel foil as a cathode to minimize cathode related variations. The uncertainty in the active material mass was extremely low (<0.1 mg), allowing us to apply constant areal current density to the anode. The cycling performances and coulombic efficiencies of Zn–V_2O_5 and Au NPs|Zn–V_2O_5 full cells, shown in Fig. S19(a), show that the specific capacity of both cells decayed primarily due to the dissolution of the cathode after the initial activation processes. In both cases, a maximum capacity of 225 mAh g^{-1} was reached, but the introduction of sparse Au NPs delivered faster activation of the cell than that observed with the bare Zn anode, resulting from the accelerated charge transfer kinetics at the surface. For the bare Zn anode, an initial soft short-circuit occurred at 334 cycles, and the severe instability of capacity curve presented at around 643 cycles, indicating the cell failure possibly due to the inhomogeneous plating on bare Zn. In sharp contrast, the Au NPs|Zn anode showed neither evidence of capacity fluctuation nor instability throughout the cycling test and a slower decaying trend was observed compared to the cell with bare Zn. This resulted in capacity retentions of 63% and 75% for the cell with bare Zn and Au NPs|Zn, respectively, evaluated between 315 and 640 cycles, which represents the onset of decay until the cell with bare Zn failed. Moreover, Au NPs|Zn contributed to a higher coulombic efficiency showing overall 99.7% compared to 99.3% for bare Zn. The charge–discharge curves of the cells with bare Zn and Au NPs|Zn (Fig. S19(b) and (c)) at selected cycles demonstrate that capacity fading was reduced by incorporating sparse Au NPs.

Overall, our results show that applying a sparse submonolayer array of Au NPs to Zn anodes provides multiple performance advantages compared to both bare Zn and sputtered Au films. The colloidal reverse micelle templating process produces small, uniformly isolated Au NPs that act as evenly distributed nucleation seeds for Zn plating. This distribution differs fundamentally from both densely coated and unstructured nanoparticle surfaces, where aggregation can create random particle sizes and uneven charge distribution. The dispersed Au NPs homogenize local electric fields on the Zn surface, generating an ion-pumping effect that lowers adsorption barriers and promotes uniform ion transport. By suppressing two-dimensional migration of Zn adatoms, the Au NPs effectively prevent rapid dendritic growth.

Electrochemical testing confirmed that Zn electrodes modified with Au NPs exhibit uniform electroplating during charge/discharge cycles, while simultaneously suppressing hydrogen evolution and corrosion at the Zn surface. The incorporation of localized Au NPs, together with plasma treatment, extends the density of active sites and enhances charge transfer kinetics, leading to a lowered nucleation barrier and improved stability in symmetric coin cells. Importantly, DFT calculations reveal that isolated Au NPs strengthen the interaction with Zn adsorbates and constrain surface diffusion more effectively than continuous Au layers, providing a mechanistic rationale for why sparse arrays outperform the full coatings reported in the literature. Consistent results were also observed in full cells, where Au NP-modified anodes showed faster activation, higher coulombic efficiency, and less capacity fading compared to bare Zn. As a result, Au NP-modified electrodes demonstrate superior performance while relying on only a minimal amount of gold introduced by a simple, solution-based method. Notably, the lifetime enhancements achieved here are substantially greater than those reported for most other interlayer materials, and are obtained without the need for high-vacuum deposition, confirming that reverse micelle-templated Au NP decoration provides highly efficient stabilization of Zn cycling with only a minimal amount of material.

4 Conclusion

In summary, we propose a novel strategy to significantly enhance the cycling stability of Zn anodes by applying a sparse submonolayer array of Au NPs for surface nanostructuring. Au NPs deposited from reverse micelle template solutions provide stable cycling while using an extremely small amount of gold, making the approach cost-effective and compatible with large-scale production. Unlike fully covered films, this modification preserves the active Zn surface in contact with the electrolyte, while leveraging the high performance of Au interlayers to reduce internal resistance and extend anode lifetime.

With the ability to tune particle size and coverage through reverse micelle templating, this solution-based process offers a promising pathway toward stable, long-life Zn batteries. These findings suggest that nanoparticle-based surface decoration may provide new opportunities to design electrode interfaces that unlock interfacial behaviors not accessible through conventional dense coatings.

Author contributions

S. I. Lee: conceptualization, experiments, methodology, data analysis, visualization, DFT calculations, writing original draft. P. Oliveira: experiments, visualization and reviewing. M. Shamekhi: data analysis, DFT calculations and reviewing. R. R. Manickam: data curation and reviewing. W. Y. Kim and J. H. Kim: resources and funding acquisition. A. Turak: resources and funding acquisition, reviewing, editing original draft and supervision.

Conflicts of interest

There are no conflicts of interest to declare.

Data availability

All data supporting the findings of this study are available from the corresponding author upon reasonable request.

Data supporting this article are also provided in the supplementary information (SI). Supplementary information: details of the experimental and simulation conditions; spatial statistics and GiSAXS analysis of the distribution of Au nanoparticles on surfaces; AFM micrographs of Zn electrode surfaces; calculated DOS of Au clusters; calculated possible absorption energies and positions on Zn surface; charge difference mapping of surfaces; AFM/SEM micrographs of RMD nanoparticles on various surfaces of different surface energies, with accompanying contact angle measurements; chronoamperometry of coin cells; Tafel curves; SEM micrographs of galvanostatic plating; synchrotron obtained X-ray scattering of Au nanoparticles, SEM micrographs of electrode surfaces showing active areas; HER tests; contact angle measurements; AFM micrographs and height distributions of RMD nanoparticles with different loading ratios; galvanostatic performance of AuNPs|Zn surface with larger nonuniform particles and the O_2PT|Zn surface; SEM micrographs of disassembled symmetric cells after failure; galvanostatic charging/discharging profile Au NPs|Zn symmetric cells under harsh conditions; full cell results; cost comparison calculations; table of comparative performance from state of the art strategies for dendrite mitigation. See DOI: https://doi.org/10.1039/d5ta08137h.

Acknowledgements

The authors thank Concordia Centre for NanoScience Research (CeNSR) at University and McMaster Centre for Advanced Light Microscopy (CALM) for AFM access; CeNSR and McMaster Centre for Advanced Nuclear Science (CANS) for SEM measurements, OCCAM for XPS measurements, and Prof. Drew Higgins for coin-cell fabrication and EIS measurement accesses. X-ray scattering measurements were performed in the Brockhouse sector of the Canadian Light Source. A. T. acknowledges financial support from the Natural Science and Engineering Research Council of Canada (Discovery Grant, RGPIN-2019-05994), the Concordia University (Faculty Development Grant 300010308), the Functional NanoMaterials Research Consortium (FMRC) and A-PRO Co., Ltd.

Notes and references

1 Z. Yi, G. Chen, F. Hou, L. Wang and J. Liang, *Adv. Energy Mater.*, 2021, **11**, 2003065.
2 S. W. Gourley, R. Brown, B. D. Adams and D. Higgins, *Joule*, 2023, **7**, 1415–1436.
3 Q. Yang, Q. Li, Z. Liu, D. Wang, Y. Guo, X. Li, Y. Tang, H. Li, B. Dong and C. Zhi, *Adv. Mater.*, 2020, **32**, 2001854.
4 K.-H. Chen, K. N. Wood, E. Kazyak, W. S. LePage, A. L. Davis, A. J. Sanchez and N. P. Dasgupta, *J. Mater. Chem. A*, 2017, **5**, 11671–11681.
5 V. Jabbari, T. Foroozan and R. Shahbazian-Yassar, *Adv. Energy Sustain. Res.*, 2021, **2**, 2000082.
6 J. Yang, R. Zhao, Y. Wang, Z. Hu, Y. Wang, A. Zhang, C. Wu and Y. Bai, *Adv. Funct. Mater.*, 2023, **33**, 2213510.
7 S.-J. Yang, L.-L. Zhao, Z.-X. Li, P. Wang, Z.-L. Liu, J. Shu and T.-F. Yi, *Coord. Chem. Rev.*, 2024, **517**, 216044.
8 Y. Yin, S. Wang, Q. Zhang, Y. Song, N. Chang, Y. Pan, H. Zhang and X. Li, *Adv. Mater.*, 2020, **32**, 1906803.
9 Q. Lu, C. Liu, Y. Du, X. Wang, L. Ding, A. Omar and D. Mikhailova, *ACS Appl. Mater. Interfaces*, 2021, **13**, 16869–16875.
10 L. Kang, M. Cui, F. Jiang, Y. Gao, H. Luo, J. Liu, W. Liang and C. Zhi, *Adv. Energy Mater.*, 2018, **8**, 1801090.
11 Y. Liu, T. Guo, Q. Liu, F. Xiong, M. Huang, Y. An, J. Wang, Q. An, C. Liu and L. Mai, *Mater. Today Energy*, 2022, **28**, 101056.
12 X. Cai, W. Tian, Z. Zhang, Y. Sun, L. Yang, H. Mu, C. Lian and H. Qiu, *Adv. Mater.*, 2024, **36**, 2307727.
13 M. Cui, Y. Xiao, L. Kang, W. Du, Y. Gao, X. Sun, Y. Zhou, X. Li, H. Li, F. Jiang and C. Zhi, *ACS Appl. Energy Mater.*, 2019, **2**, 6490–6496.
14 Q. Ren, X. Tang, X. Zhao, Y. Wang, C. Li, S. Wang and Y. Yuan, *Nano Energy*, 2023, **109**, 108306.
15 H. J. Kim, S. Kim, S. Kim, S. Kim, K. Heo, J.-H. Lim, H. Yashiro, H.-J. Shin, H.-G. Jung, Y. M. Lee and S.-T. Myung, *Adv. Mater.*, 2024, **36**, 2308592.
16 S. Zhao, Y. Zhang, J. Li, L. Qi, Y. Tang, J. Zhu, J. Zhi and F. Huang, *Adv. Mater.*, 2023, **35**, 2300195.
17 Z. Yang, C. Lv, W. Li, T. Wu, Q. Zhang, Y. Tang, M. Shao and H. Wang, *Small*, 2022, **18**, 2104148.
18 Y. Dai, C. Zhang, W. Zhang, L. Cui, C. Ye, X. Hong, J. Li, R. Chen, W. Zong, X. Gao, J. Zhu, P. Jiang, Q. An, D. J. L. Brett, I. P. Parkin, G. He and L. Mai, *Angew. Chem., Int. Ed.*, 2023, **62**, e202301192.
19 J. Q. Lu and S. S. Yi, *Langmuir*, 2006, **22**, 3951–3954.
20 S. I. Lee, M. Munir, R. Arbi, P. Oliveira, S. J. Lee, J. H. Lim, W. Y. Kim and A. Turak, *J. Mater. Sci.: Mater. Electron.*, 2023, **34**, 1101.
21 M. Munir, R. Arbi, J. Tan, P. Oliveira, S. I. Lee, M. C. Scharber, N. S. Sariciftci, F. Xu, G. Xu and A. Turak, *ACS Appl. Nano Mater.*, 2024, **7**, 5405–5413.
22 A. Turak, *id. Proc. Adv. Mater.*, 2021, **2**, 2103166.
23 P. Q. Oliveira, R. Arbi, M. Munir, L. Patil and A. Z. Turak, *Flexible Printed Electron.*, 2024, **9**, 025019.
24 D. Nečas and P. Klapetek, *Open Phys.*, 2012, **10**, 181–188.
25 A. F. G. Leontowich, A. Gomez, B. Diaz Moreno, D. Muir, D. Spasyuk, G. King, J. W. Reid, C.-Y. Kim and S. Kycia, *J. Synchrotron Radiat.*, 2021, **28**, 961–969.
26 B. H. Toby and R. B. Von Dreele, *J. Appl. Crystallogr.*, 2013, **46**, 544–549.
27 T. H. Wan, M. Saccoccio, C. Chen and F. Ciucci, *Electrochim. Acta*, 2015, **184**, 483–499.
28 M. Bumstead, K. Liang, G. Hanta, L. S. Hui and A. Turak, *Sci. Rep.*, 2018, **8**, 1554.
29 J. Enkovaara, C. Rostgaard, J. J. Mortensen, J. Chen, M. Dułak, L. Ferrighi, J. Gavnholt, C. Glinsvad, V. Haikola, H. A. Hansen, H. H. Kristoffersen, M. Kuisma, A. H. Larsen, L. Lehtovaara, M. Ljungberg, O. Lopez-Acevedo, P. G. Moses, J. Ojanen, T. Olsen, V. Petzold, N. A. Romero, J. Stausholm-Møller,

M. Strange, G. A. Tritsaris, M. Vanin, M. Walter, B. Hammer, H. Häkkinen, G. K. H. Madsen, R. M. Nieminen, J. K. Nørskov, M. Puska, T. T. Rantala, J. Schiøtz, K. S. Thygesen and K. W. Jacobsen, *J. Phys.: Condens. Matter*, 2010, **22**, 253202.

30 L. G. V. Briquet, M. Sarwar, J. Mugo, G. Jones and F. Calle-Vallejo, *ChemCatChem*, 2017, **9**, 1261–1268.

31 P. E. Blöchl, *Phys. Rev. B: Condens. Matter Mater. Phys.*, 1994, **50**, 17953–17979.

32 G. Henkelman and H. Jónsson, *J. Chem. Phys.*, 2000, **113**, 9978–9985.

33 Q. Hu, K. Gao, X. Wang, H. Zheng, J. Cao, L. Mi, Q. Huo, H. Yang, J. Liu and C. He, *Nat. Commun.*, 2022, **13**, 3958.

34 J. Kim, J. K. Seo, J. Song, S. Choi, J. Park, H. Park, J. Song, J.-H. Noh, G. Oh, M. H. Seo, H. Lee, J. M. Lee, I.-C. Jang, J. Kim, H.-J. Kim, J. Ma, J. Cho and J.-J. Woo, *Adv. Energy Mater.*, 2024, **14**, 2401820.

35 M. Bumstead, K. Liang, G. Hanta, L. S. Hui and A. Turak, *Sci. Rep.*, 2018, **8**, 1554.

36 M. Qiu, H. Liu, J. Luo, B. Tawiah, S. Fu and H. Jia, *Chem. Commun.*, 2022, **58**, 993–996.

37 X. Liu, X. Wang, J. Yao, J. Li, Y. Gan, Z. Wu, J. Zheng, W. Hao, L. Lv, L. Tao, J. Zhang, H. Wang, X. Ji, H. Wan and H. Wang, *Adv. Energy Mater.*, 2024, **14**, 2400090.

38 Y. Song, Y. Liu, S. Luo, Y. Yang, F. Chen, M. Wang, L. Guo, S. Chen and Z. Wei, *Adv. Funct. Mater.*, 2024, **34**, 2316070.

39 R. Zhu, Z. Xiong, H. Yang, T. Huang, S. Jeong, D. Kowalski, S. Kitano, Y. Aoki, H. Habazaki and C. Zhu, *Energy Storage Mater.*, 2022, **46**, 223–232.

40 M. Kim, J. Lee, Y. Kim, Y. Park, H. Kim and J. W. Choi, *J. Am. Chem. Soc.*, 2023, **145**, 15776–15787.

41 P. Cao, J. Tang, A. Wei, Q. Bai, Q. Meng, S. Fan, H. Ye, Y. Zhou, X. Zhou and J. Yang, *ACS Appl. Mater. Interfaces*, 2021, **13**, 48855–48864.

42 L. A. Kibler, J. M. Hermann, A. Abdelrahman, A. A. El-Aziz and T. Jacob, *Curr. Opin. Electrochem.*, 2018, **9**, 265–270.

43 C. Ma, A. Nikiforov, D. Hegemann, N. De Geyter, R. Morent and K. K. Ostrikov, *Int. Mater. Rev.*, 2023, **68**, 82–119.

44 K. Wang, J. Hu, T. Chen, K. Wang, J. Wu, Q. Chen, Z. Deng and W. Zhang, *ACS Sustain. Chem. Eng.*, 2023, **11**, 9111–9120.

45 Y. Lin, Z. Mai, H. Liang, Y. Li, G. Yang and C. Wang, *Energy Environ. Sci.*, 2023, **16**, 687–697.

46 S.-B. Wang, Q. Ran, R.-Q. Yao, H. Shi, Z. Wen, M. Zhao, X.-Y. Lang and Q. Jiang, *Nat. Commun.*, 2020, **11**, 1634.

47 S. Li, Z. Li, L. Huai, M. Ma, K. Luo, J. Chen, D. Wang and Z. Peng, *J. Energy Chem.*, 2021, **62**, 179–190.

48 P. Samanta, S. Ghosh, A. Kundu, H. Kolya, C.-W. Kang, P. Samanta, N. C. Murmu and T. Kuila, *ACS Sustain. Chem. Eng.*, 2023, **11**, 5495–5505.

49 Y. Dai, C. Zhang, W. Zhang, L. Cui, C. Ye, X. Hong, J. Li, R. Chen, W. Zong, X. Gao, J. Zhu, P. Jiang, Q. An, D. J. L. Brett, I. P. Parkin, G. He and L. Mai, *Angew. Chem., Int. Ed.*, 2023, **62**, e202301192.

50 Z. Cai, F. Zhang, M. Zhou, W. Sun and H. Pan, *J. Power Sources*, 2024, **603**, 234402.

51 Y. Wang, C. Ye, J. Wang, F. Chen, J. Qian, C. Yang, Y. Song, L. Bi, Q. Xie, L. He, J. Yu, X. Wei, H. Song, J. Liao, S. Wang and R. Chen, *Nano Energy*, 2024, **119**, 109093.

52 K. Bai, X. Wang, J. Ke, Z. Wen, Z. Hu, W. Du, Y. Zhang, M. Ye, Y. Tang, X. Liu, L. Niu and C. Chao Li, *Angew. Chem., Int. Ed.*, 2025, **64**, e202423138.

53 D. James Martin, D. Decarolis, Y. I. Odarchenko, J. J. Herbert, T. Arnold, J. Rawle, C. Nicklin, H.-G. Boyen and A. M. Beale, *Chem. Commun.*, 2017, **53**, 5159–5162.

54 G. Pramanik, J. Humpolickova, J. Valenta, P. Kundu, S. Bals, P. Bour, M. Dracinsky and P. Cigler, *Nanoscale*, 2018, **10**, 3792–3798.

55 K. Lewis, R. Arbi, A. Ibrahim, E. Smith, P. Olivera, F. Garza and A. Turak, *J. Mater. Sci.: Mater. Electron.*, 2023, **34**, 750.

56 J. Zhao, S. Gu, X. Xu, T. Zhang, Y. Yu, X. Di, J. Ni, Z. Pan and X. Li, *Catal. Sci. Technol.*, 2016, **6**, 3263–3270.

57 I. R. Milošević, B. Vasić, A. Matković, J. Vujin, S. Aškrabić, M. Kratzer, T. Griesser, C. Teichert and R. Gajić, *Sci. Rep.*, 2020, **10**, 8476.

58 M. Wu, W.-J. Chen, Y.-H. Shen, F.-Z. Huang, C.-H. Li and S.-K. Li, *ACS Appl. Mater. Interfaces*, 2014, **6**, 15052–15060.

59 Y. Cheng, S. Lu, W. Xu, H. Wen and J. Wang, *J. Mater. Chem. A*, 2015, **3**, 16774–16784.

60 K. Zou, P. Cai, X. Deng, B. Wang, C. Liu, Z. Luo, X. Lou, H. Hou, G. Zou and X. Ji, *Chem. Commun.*, 2021, **57**, 528–531.

61 J. Y. Kim, G. Liu, G. Y. Shim, H. Kim and J. K. Lee, *Adv. Funct. Mater.*, 2020, **30**, 2004210.

62 H. Peng, X. Wang, Z. Liu, H. Lei, S. Cui, X. Xie, Y. Hu and G. Ma, *ACS Appl. Mater. Interfaces*, 2023, **15**, 4071–4080.

63 W. Wen, J.-M. Wu and Y.-D. Wang, *Sens. Actuators, B*, 2013, **184**, 78–84.

64 H. Lu, D. Zhang, Q. Jin, Z. Zhang, N. Lyu, Z. Zhu, C. Duan, Y. Qin and Y. Jin, *Adv. Mater.*, 2023, **35**, 2300620.

65 W. Xu, K. Zhao, W. Huo, Y. Wang, G. Yao, X. Gu, H. Cheng, L. Mai, C. Hu and X. Wang, *Nano Energy*, 2019, **62**, 275–281.

66 Y. Zeng, X. Zhang, R. Qin, X. Liu, P. Fang, D. Zheng, Y. Tong and X. Lu, *Adv. Mater.*, 2019, **31**, 1903675.

67 S. I. Kim and T. D. Chung, *Anal. Chem.*, 2024, **96**, 3096–3106.

68 E. J. Hansen, Z. Wu, T. Olfatbakhsh, A. Milani and J. Liu, *J. Membr. Sci.*, 2023, **688**, 122130.

69 W. Guo, Y. Zhang, X. Tong, X. Wang, L. Zhang, X. Xia and J. Tu, *Mater. Today Energy*, 2021, **20**, 100675.

70 H. Wu, W. Yan, Y. Xing, L. Li, J. Liu, L. Li, P. Huang, C. Lai, C. Wang, W. Chen and S. Chou, *Adv. Funct. Mater.*, 2024, **34**, 2213882.

71 Y. Ding, M. Guo, S. Lu, T. Liu, Q. Shen, J. Ying, Y. Wang and Z. Yu, *J. Mater. Chem. A*, 2025, **13**, 18560–18570.

72 M. Sun, Q. Cheng, X. Ren, N. Wang, L. Hu, Z. Gan, Y. Xiang, Z. Yan, C. Jia and Z. Li, *Adv. Funct. Mater.*, 2025, **35**, 2413456.

73 World Bank, *Average Prices for Gold Worldwide from 2014 to 2024 with a Forcast to 2026 (in Nominal U.S. Dollars per Troy Ounce)*, Statista Inc., 2025, https://www.statista.com/statistics/675890/average-prices-gold-worldwide/, accessed January 27, 2026.

74 D. Kundu, B. D. Adams, V. Duffort, S. H. Vajargah and L. F. Nazar, *Nat. Energy*, 2016, **1**, 16119.

75 S. Orangi, N. Manjong, D. P. Clos, L. Usai, O. S. Burheim and A. H. Strømman, *J. Energy Storage*, 2024, **76**, 109800.